Stability Analysis of Tendon Driven Continuum Robots and Application to Active Softening

Quentin Peyron[1,2], *Member, IEEE*, and Jessica Burgner-Kahrs[1], *Senior Member, IEEE.*

***Abstract*—Tendon driven continuum robots are often considered to navigate through- and operate in cluttered environments. While their compliance allows them to conform safely to obstacles, it leads them also to buckle under tendon actuation. In this work, we perform for the first time an extensive elastic stability analysis of these robots for arbitrary planar designs. The buckling phenomena are investigated and analyzed using bifurcation diagrams, complementing the current state of the art and adding new knowledge about robots composed of n spacer disks. We show the existence of multiple robot configurations with different shapes, achievable with the same actuation inputs. A global stability criterion is also established which links the critical tendon force, until which the robot is stable, to the design parameters. Finally, the buckling phenomena are used to actively soften the robot for a better compromise between compliance and payload. An open loop control strategy is proposed, which can theoretically decrease the stiffness to zero while maintaining the same robot shape. Experimentally, the robot is made 4 times more compliant than it is nominally using tendon actuation only.**

***Index Terms*—Tendon/Wire Mechanisms, Modeling, Control and Learning for Soft Robots, Kinematics, Elastic Stability of Continuum Robots**

I. Introduction

Tendon driven continuum robots (TDCR) are one of the first and most considered type of continuum robot today. They consist of a slender elastic backbone, deformed by pulling on and releasing tendons to generate motion. The tendons are commonly guided along the backbone using rigid spacer disks, at a specific distance from it. As a result, pulling on the tendons generate forces and moments on the disks, which result in the bending of the backbone. TDCR have several properties which make them particularly interesting for operating in constrained and sensitive environments. They can be designed and controlled to conform to curvilinear shapes and navigate through tortuous pathways or around obstacles. The number of tendons and their routing along the backbone can be chosen to obtain curves with a desired number of inflection points [1] or with helical shapes [2]. They can be controlled to perform follow-the-leader deployments [3], [4]. Also, their natural compliance allow them eventually to deform when contacting the environment instead of damaging it. As a consequence, they have been largely considered for minimally invasive surgery [5], where the human body constitutes a constrained and fragile environment. However, due to their flexibility, TDCR and other continuum robots are challenging to use for two reasons: they can experience elastic stability issues and their design involves a compromise between load bearing capabilities and compliance.

Elastic stability issues of continuum robots arise from buckling of the slender backbone under the applied actuation forces and/or external forces. They have been mostly observed and studied for concentric tube continuum robots [6]–[8]. The relative rotation of telescopic pre-curved tubes leads to the accumulation of torsional deformation energy. Past a certain critical rotation, rotating the tubes further leads to a sudden release of this energy. The robot becomes elastically unstable and generates a snapping motion which is difficult to control and dangerous for its surrounding. This phenomenon is similar to the buckling of cantilever beams, as explained in [7]. Unstable phenomena appear for lengths of tubes beyond a critical interaction length, whose value is related to the tube's mechanical and geometrical properties. Past this global stability limit, the robot can have multiple configurations for the same actuation inputs and snap between these configurations [8]. Knowing the relation between this stability limit and the design parameters allows to avoid unstable phenomena through tube design [9] and path planning [10]. Elastic stability issues have also been reported for magnetic continuum robots [11]–[13], which depend on the backbone mechanical and magnetic properties and the applied magnetic fields.

Although it has been rarely observed or discussed in the literature, TDCR can also be subject to buckling. Pulling on all the tendons simultaneously will compress the elastic backbone and lead to losses of elastic stability eventually. To avoid this, the current practice is to limit the pre-tension on the tendons or to limit the tendon tension through control. However, there exists no criterion, to the best of our knowledge, that indicates the critical tendon force above which buckling appears. These phenomena have been observed for TDCR in the early work of Li and Rahn [14]. They considered a planar robot composed of one disk at the tip, to which one tendon is attached. By solving a model tailored to the 1-disk planar TDCR, and by conducting experiments, they showed that the robot can have up to two different stable configurations beyond a certain tendon force. However, this phenomenon was not studied in detail. The authors showed that the critical tendon force above which multiple shapes exist depends on the robot design parameters, such as the end-disk radius, but did not provide an analytical stability criterion. Moreover, the results are specific to a planar TDCR composed of one disk.

As a second challenge, the elasticity of TDCR requires a compromise between their load bearing capabilities and

This work was supported by the H2020 EU SimCardioTest project (Digital transformation in Health and Care SC1-DTH-06-2020; grant agreement No. 101016496

[1]Continuum Robotics Laboratory, Department of Mathematical & Computational Sciences, University of Toronto, ON, Canada

[2]DEFROST Team, Inria and CRIStAL UMR CNRS 9189, University of Lille, Villeneuve d'Ascq, France

quentin.peyron@inria.fr

compliance during their design. On one hand, generating a force at the robot tip requires the robot to be stiff. On the other hand, being able to contact the environment without damaging it requires it to be compliant. In order to deal with this trade-off, two approaches have been considered in the literature which can be qualified as control-based and design-based. Control-based approaches consist in using position force control strategies to vary the robot stiffness at its end-effector [15], [16]. These methods regulate the end-effector stiffness indirectly by closing a position loop to respond to external force disturbance and control the end-effector stiffness. They allow to significantly increase or decrease the natural tip stiffness in desired directions. However, they require multiple actuated degrees of freedom to control both the tip position and force which result typically in complex actuation units.

Alternatively, a body of work has been focusing on designing stiffening and softening actuation principles for continuum robots. These principles involve several mechanisms such as layer and granular jamming [17], [18], shape memory material and low-melting point alloy (LMPA) [19], and antagonistic actuation [20]. In this last work, tendons are used to lock the expansion of a pneumatic chamber and increase the apparent stiffness of the structure with two discrete states. Comprehensive reviews of the different principles can be found in [21], [22]. They don't allow to vary the stiffness along specific directions, but can vary the stiffness globally without changing the robot shape and with a minimal number of actuation inputs. Active increase or decrease of the backbone stiffness with ratios reaching several tens have been achieved. However, these strategies come with their own challenges. Adding antagonistic actuators dedicated to stiffness modulation or jamming sheath increases the diameter of the robot. Jamming mechanisms and LMPA rely on friction and glass transition of material, which are physical phenomena difficult to control. They are mainly used to achieve two discrete states, stiff and soft. Shape memory material and LMPA require temperature control, whose bandwidth is often limited.

The apparent stiffness of an elastic structure can be changed by applying forces and making it closer or farther to buckling. Increasing the forces applied on a beam increases its elastic energy and brings it closer to its stability limit. As a result, the beam is more easily deformed under the action of an external force. Its compliance to this force is then larger. This principle has been used to realize compliant mechanisms, whose stiffness can be varied with large amplitudes and bandwidth [23]–[25]. The buckled element is realized using compression springs in [25] and pre-strained leaf springs in [23], [24]. Buckling has also been used to modulate the stiffness and improve the behaviour of soft devices [26], leveraging primarily pneumatic and tensile actuation with specific beam arrangements and spatial geometries. It has been recently considered to amplify the motion of continuum robots actuated with electro-active polymers in [27]. The continuum robot is deformed by a pair of antagonistic tensile actuators, that compress the elastic backbone. A TDCR can exhibit the same amplification principle, as it is naturally composed of antagonistic tendons to achieve bidirectional bending. As a consequence, the buckling phenomena induced by tendon actuation offer a unique opportunity to actively reduce the TDCR stiffness. In particular, it would allow to achieve continuous stiffness variations without adding actuators, and therefore without increasing the robot diameter. Also, it would only use electro-mechanical actuators to pull on the tendons, which can have a higher bandwidth than temperature regulated systems and are easier to control.

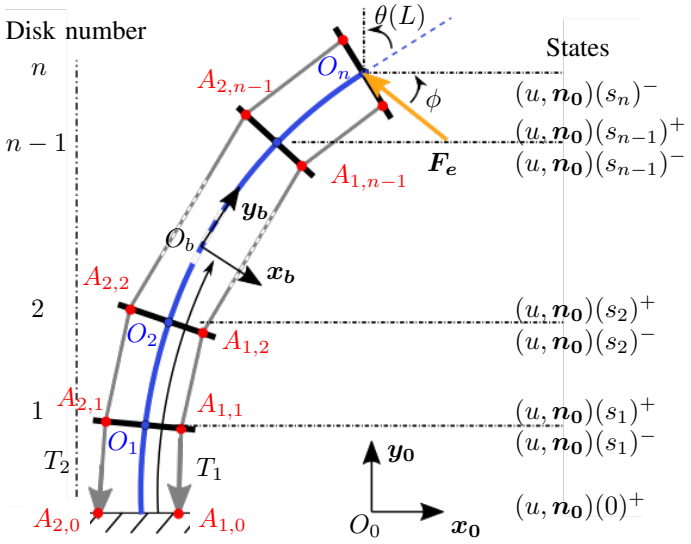

Fig. 1: Schematics of the planar TDCR. The elastic backbone is represented in blue, the tendons in grey and the disks in black. The tendon holes are depicted with red dots. The robot is subject to an external force applied on its tip represented in orange.

The contributions of this paper are as followed:

- The elastic stability issues for planar TDCR are investigated numerically and experimentally, bringing insights on the results of the 1-disk TDCR [14] and extending these results to designs with more disks.
- An analytical global stability criterion relating the design parameters to critical actuation values is developed.
- The buckling phenomena induced by tendon actuation are used to achieve active softening for the first time. Softening is achieved instead of stiffening [20] due to the absence of antagonistic pneumatic chambers and the control of tendon tension instead of displacement.

The paper is organized as follows. The static model of TDCR, the numerical method used to analyze the stability and the experimental setup for the validation of the model and the stiffness modulation are described in Sec.II. The results of the stability analysis are presented in Sec.III and in Sec.IV for the 1-disk and n-disks TDCR cases respectively. Finally, the buckling-based active softening strategy is investigated in Sec.V, before concluding.

II. Method and Material

A. Forward and Inverse Static Model

We consider the case of a planar TDCR as represented on Fig. 1. It is composed of an elastic backbone, deformed by

two antagonistic tendons guided through n spacer disks and attached to the last one. Additionally, the spacer disks delimit n subsegments along the robot. To model the continuum manipulator statics, we consider classical assumptions for TDCR composed of spacer disks [28]. The backbone is assumed to behave as a Kirchhoff rod, where the backbone elongation and shear are neglected, which is true for long and slender elastic beams. The disk thickness is assumed to be small with respect to the robot length and is, therefore, neglected. Additionally, we neglect the mechanical clearance between the tendons and their respective guiding holes on the disk. As a consequence, the disks exert point-wise constraints on the tendons and do not have an influence on the backbone stiffness. The tendons are thus partially constrained along the backbone at the disk locations. The robot is assumed to be subject to an external force applied at its tip, which might happen when in contact with the environment or due to the weight of manipulated objects. The weight of the robot backbone is neglected.

The TDCR is modeled using the variable curvature model with partially constrained tendons described in [29], reformulated with the planar Kirchhoff rod assumption. The robot backbone is parametrized by its arc length s. A local frame $\mathcal{R}_b = (O_b, \boldsymbol{x_b}, \boldsymbol{y_b})$ is attached to the backbone at s, where $\boldsymbol{y_b}$ is tangent to the backbone centerline. The pose of $\mathcal{R}_b$ with respect to a fixed reference frame $\mathcal{R}_0 = (O_0, \boldsymbol{x_0}, \boldsymbol{y_0})$ for all s defines the pose of the TDCR in the plane. In particular, the robot position and orientation are represented respectively by the planar Cartesian coordinates $\boldsymbol{p}(s)$ of O_b in $\mathcal{R}_0$ and the bending angle between $\boldsymbol{y_0}$ and $\boldsymbol{y_b}$, denoted $\theta(s)$. They are linked to the robot curvature $u(s)$ by the relation:

$$\begin{aligned} \theta'(s) &= u(s) \\ \boldsymbol{p'}(s) &= {}^{\boldsymbol{0}}\boldsymbol{R_b}\boldsymbol{v} \end{aligned} \tag{1}$$

where $[...]'$ denotes the derivative with respect to s, $\boldsymbol{v} = \begin{bmatrix} 0 & 1 \end{bmatrix}^T$ and ${}^{\boldsymbol{0}}\boldsymbol{R_b} \in SO(2)$ is the rotation matrix from $\mathcal{R}_b$ to $\mathcal{R}_0$. The robot curvature depends on the action of tendons and the external tip force through the internal forces $\boldsymbol{n_0}(s)$ expressed in $\mathcal{R}_0$. It is obtained by integrating the following differential equations:

$$\begin{aligned} u'(s) &= (EI)^{-1}\boldsymbol{v^T}\left({}^{\boldsymbol{b}}\boldsymbol{R_0}\boldsymbol{n_0}(s)\right) \\ \boldsymbol{n_0'}(s) &= \boldsymbol{0} \end{aligned} \tag{2}$$

where E is the young modulus of the material composing the backbone, I is the second moment of area of the cross-section, and $\boldsymbol{n_0}(s)$ is the vector of distributed internal force along the backbone.

The tendons and the interactions at the tip exert forces and moments at the disk location along the backbone, which is equal to $s_i = iL/n$ for disk i, with $i = \{0, ..., n\}$. These forces and moments depend on the position of the tendon holes on each disk, which are represented by points denoted $A_{j,i}$ for tendon j on disk i as depicted in Fig. 1. The tendon holes are placed at a distance r_d from the backbone, so that $A_{1,i} = \begin{bmatrix} r_d & 0 \end{bmatrix}^T$ and $A_{2,i} = \begin{bmatrix} -r_d & 0 \end{bmatrix}^T$ with respect to $\mathcal{R}_b$ at s_i. The direction of tendon j between disks $i-1$ and i is denoted $\boldsymbol{a_{j,i}} = \overrightarrow{A_{j,i-1}A_{j,i}} / \left|\overrightarrow{A_{j,i-1}A_{j,i}}\right|$. The forces and moments are then obtained using the relation:

$$\begin{aligned} \boldsymbol{f}_{j,i} &= \begin{cases} -T_{j,i}\boldsymbol{a_{j,i}} + T_{j,i+1}\boldsymbol{a_{j,i+1}}, i < n \\ T_{j,i}\boldsymbol{a_{j,i}} + \boldsymbol{f}_e \qquad i = n \end{cases} \\ m_{j,i} &= \overrightarrow{O_iA_{j,i}}^T \boldsymbol{f}_{j,i} \end{aligned} \tag{3}$$

where $T_{j,i}$ is the tendon tension along sub-segment i and $\boldsymbol{f}_e = \begin{bmatrix} F_e\cos(\phi) & F_e\sin(\phi) \end{bmatrix}^T$ is the external tip force of magnitude F_e and orientation ϕ. The tendon tension varies between the subsegments because of the friction between the tendons and the disks. These frictions are modeled using the Coulomb friction law as proposed in [29]. Let μ be the static friction coefficient, the tendon tension can be computed recursively using:

$$T_{j,i+1} = T_{j,i}\frac{1 + \mu\,\boldsymbol{a_{j,i}^T}\boldsymbol{x_{b,i}}}{1 + \mu\,\boldsymbol{a_{j,i+1}^T}\boldsymbol{x_{b,i}}} \tag{4}$$

where $\boldsymbol{x_{b,i}} = \boldsymbol{x_b}(s_i)$. We also assume that the forces along $\boldsymbol{y_b}$ exerted by the tendons on disks $i < n$ can only be due to friction [28]. The tendon forces and moments, as well as the external force at the tip, appear as boundary conditions of the system (2):

$$\begin{aligned} u(s_i)^+ &= u(s_i)^- + (EI)^{-1}(m_{1,i} + m_{2,i}) \\ \boldsymbol{n_0}(s_i)^+ &= \boldsymbol{n_0}(s_i)^- + \boldsymbol{f}_{1,i} + \boldsymbol{f}_{2,i} \end{aligned} \tag{5}$$

where $u(s_i)^+$ and $u(s_i)^-$ are equal to $\lim_{s\to s_i} u(s)$ with $s > s_i$ and $s < s_i$. Similarly, $\boldsymbol{n_0}(s_i)^+$ and $\boldsymbol{n_0}(s_i)^-$ are equal to $\lim_{s\to s_i} \boldsymbol{n_0}(s)$ with $s > s_i$ and $s < s_i$.

The forward and inverse static problems are solved using a shooting method. The forward static problem aims at finding the robot configuration from the tension applied on each tendon. The values of u and $\boldsymbol{n_0}$ at the beginning of each subsegment are guessed and iterated until the boundary conditions (5) are satisfied. The forward static problem consists thus in finding the solution $\boldsymbol{x}$ of the set of $3n$ nonlinear equations $\boldsymbol{g_F} = \begin{bmatrix} \boldsymbol{g_{F1}^T} & \boldsymbol{g_{F2}^T} & ... & \boldsymbol{g_{Fn}^T} \end{bmatrix}^T$, where $\boldsymbol{g_{Fi}}$ corresponds to (5) for subsegment i, of the general form:

$$\boldsymbol{g_F}(\boldsymbol{x}, T_1, T_2, F_e, \phi) = \boldsymbol{0} \tag{6}$$

where $\boldsymbol{x} = \begin{bmatrix} \boldsymbol{x_0} & \boldsymbol{x_1} & ... & \boldsymbol{x_{n-1}} \end{bmatrix}^T$ with $\boldsymbol{x_i} = \begin{bmatrix} u(s_i)^+ & (\boldsymbol{n}(s_i)^+)^T \end{bmatrix}$. This system is solved numerically using a Newton-Raphson algorithm. At each numerical step, the tendon points $A_{j,i}$, with $j = 1, 2$ and $i = \{0, ..., n\}$, and the states at the end of each subsegment are obtained by integrating (1-2) with a Runge-Kutta 45 scheme, starting from $\boldsymbol{x}$. The boundary conditions can then be evaluated.

The inverse static problem aims at finding the tendon tensions that allow to reach a desired bending angle at the robot tip while applying a desired total force on the backbone. In addition to $\boldsymbol{x}$, we iterate on the two tendon forces in order to reach a desired total tendon force T_d and a tip orientation θ_d specified by the user. This is achieved by adding the two following constraints to the boundary conditions:

$$\begin{aligned} \theta(L) &= \theta_d \\ T_1 + T_2 &= T_d \end{aligned} \tag{7}$$

Solving the inverse static problem is thus equivalent to finding the solution $\boldsymbol{y}$ to the system of non-linear equations:

$$\boldsymbol{g_I}(\boldsymbol{y}, \theta_d, T_d, F_e, \phi) = \boldsymbol{0} \tag{8}$$

where $\boldsymbol{y} = \begin{bmatrix} \boldsymbol{x} & T_1 & T_2 \end{bmatrix}$. The same numerical methods as for the forward problem are used to solve the inverse problem.

B. Numerical analysis

Studying analytically the static model of an n-disk TDCR is challenging because of the robot's non-linear behavior. Therefore, we solve and analyze the forward and inverse static model numerically. This task can be difficult when analyzing buckling phenomena. Solving (6) and (8) numerically requires a good initial guess for the algorithm to converge. As the robot shape is difficult to predict during large deformations, and can vary significantly under small variations in tendon tensions close to the unstable configurations, this initial guess can be hard to find. Also, buckling phenomena lead the system to experience branching, i.e. the model cardinality increases from one to several solutions beyond a critical buckling force. The convergence of the model towards one particular solution depends on the choice of initial guess. Also, the static models are typically singular at the branching points, inducing convergence issues with standard numerical solvers.

To deal with these problems, the static models are solved and analyzed using the numerical framework presented in [8]. It is composed of a prediction-correction continuation method, detection functions of branching points from bifurcation theory, and an elastic stability criterion. These different methods are explained in the following.

Continuation method and bifurcations analysis have been considered for the analysis of continuum robots in [8], [13]. The continuation method computes the successive configurations of the TDCR when one of the model parameters is varied, here the tendon force. The computed sets of configurations are called branches. Starting from an existing solution, the next solution is predicted by considering the branch tangent and incrementing the tension value by a specific step size. This prediction is then used as an initial guess to converge to the actual solution using a Newton method. In case the method has problems of convergence, the step size is automatically reduced and the prediction is updated. Bifurcation theory provides mathematical functions to detect the appearance of branching points (BP) and limit points (LP). The latter indicates that the branch has a vertical tangent, and therefore that the robot shape will be sensitive to small perturbations. Once these specific configurations are detected, a secant method is used to solve the static model which is robust to singularities. The numerical framework flowchart and implementation details on the continuation algorithm and the detection functions are given in [8].

The continuation method allows finding robot configurations in the continuation of a previous one, i.e. on the same branch of solution. However, several branches can exist which are disconnected from each other. Finding these branches requires finding at least one robot configuration belonging to them. To find these initial robot configurations, we solve the forward static model for a discrete set of initial guesses of $\boldsymbol{y}$. We consider $u^+(s_i) \in \{-u_{max}, 0, u_{max}\}$, where $u_{max} = r_d(T_1 + T_2)/(EI)$ is the curvature obtained when considering the tendon to apply a point moment at the robot tip. We consider also 8 different orientations for the internal force at the base of each subsegment, i.e. $\boldsymbol{n_0^+}(s_i) = (T_1 + T_2)\begin{bmatrix}\cos(\gamma) & \sin(\gamma)\end{bmatrix}$ with $\gamma \in \{0, \pi/4, ..., 7\pi/4\}$. This gives us a set of $3^n 8^n$ initial guesses for a TDCR composed of n disks. Solving the model for each of these guesses leads to a set of robot configurations. Some of them are identical, with slight shape deviations due to tolerances in the numerical integration and Newton solver, as different initial guesses can lead to the same solution. We manually eliminate these configurations from the set, as they are likely to belong to the same branch. The continuation method is applied to each of the obtained sets. Note that this method does not ensure that all robot configurations have been found, which is beyond the scope of this paper.

In addition to these methods, we use the elastic stability criterion proposed in [30] to evaluate the stability of the computed configurations. This criterion is derived from the optimal control theory for beams subject to boundary conditions at their tip. The beam configuration is stable if the derivative of the boundary conditions with respect to the internal forces and moments at a given arc length s is full rank $\forall s$. This criterion can be directly applied to a TDCR composed of one spacer disk only at its tip. In that case, and considering that the internal moment can be obtained from the backbone curvature using the linear constitutive equation of the material, a configuration is considered stable if:

$$\begin{bmatrix} \frac{1}{EI} & 0 & 0 \\ 0 & 1 & 0 \\ 0 & 0 & 1 \end{bmatrix} \frac{\partial \boldsymbol{g_{Fn}}}{\partial \boldsymbol{x_s}} \text{ is full rank } \forall s \in [0, L] \tag{9}$$

where $\boldsymbol{x_s} = \begin{bmatrix} u(s) & \boldsymbol{n}(s)^T \end{bmatrix}$. The derivative can be obtained using finite differences. After perturbating $\boldsymbol{x_s}$, the differential equations are integrated from s to the tip and the change in the boundary conditions is computed.

This criterion must be adapted to the case of robots with $n \geq 2$, as the intermediate spacer disks induce boundary conditions along the backbone, and the internal forces and curvature are guessed at the beginning of each subsegment. To do so, we consider that the state of the robot depends on the state vector $\boldsymbol{y}$ and the perturbated state $\boldsymbol{y_s}$ at s and that the intermediate boundary conditions result in constraints between these states. As a result, the robot can be considered as a beam with boundary conditions $\boldsymbol{g_{Fn}}$ at the tip only, and the respect of the intermediate constraints can be ensured by projecting the state perturbation in the constraints kernel, as classically performed for the stability analysis of elastic rods [31] and continuum robots [32]. In addition, as we integrate from s to L in the finite difference scheme, we consider that the effect of a perturbation applied along subsegment i on $\boldsymbol{g_{Fn}}$ will only be affected by the next subsegments. Therefore, when s is along subsegment i, the matrix in Eq. (9) will be impacted by the states $\boldsymbol{x^\star} = \begin{bmatrix} \boldsymbol{x_s} & \boldsymbol{x_i} & ... & \boldsymbol{x_{n-1}} \end{bmatrix}^T$ and the constraints $\boldsymbol{c} = \begin{bmatrix} \boldsymbol{g_{Fi}^T} & ... & \boldsymbol{g_{Fn-1}^T} \end{bmatrix}^T$. The derivative of $\boldsymbol{g_{Fn}}$ with respect

to all the states can then be written:

$$\frac{\partial \boldsymbol{g_{Fn}}}{\partial \boldsymbol{x^\star}} = \frac{\partial \boldsymbol{g_{Fn}}}{\partial \boldsymbol{x^\star}} N\left(\frac{\partial \boldsymbol{c}}{\partial \boldsymbol{x^\star}}\right) N\left(\frac{\partial \boldsymbol{c}}{\partial \boldsymbol{x^\star}}\right)^T \tag{10}$$

where $N(\boldsymbol{A})$ stands for the kernel of the bilinear application defined by matrix $\boldsymbol{A}$. From the right to the left, the first kernel operator projects a $3n \times 1$ perturbation vector into the constraints null-space, which is of dimension 3 since there are $3(n-i)$ constraints and $3(n-i+1)$ states. We obtain a vector of perturbations that satisfies the constraints. The second kernel operator maps these new perturbations back to the partial state space spanned by the components of $\boldsymbol{x^\star}$. The derivative of the tip boundary conditions we need for the stability evaluation corresponds finally to the three first rows of $\frac{\partial \boldsymbol{g_{Fn}}}{\partial \boldsymbol{x^\star}}$:

$$\frac{\partial \boldsymbol{g_{Fn}}}{\partial \boldsymbol{x_s}} = \frac{\partial \boldsymbol{g_{Fn}}}{\partial \boldsymbol{x^\star}} \left[\mathbb{I}_{3\times 3} \quad \mathbb{O}_{3\times 3(n-i)}\right] \tag{11}$$

The criterion is evaluated numerically by discretizing each subsegment with 20 nodes. The derivatives are then evaluated at each node using finite differences, resulting in $20n$ 3×3 matrices. Losses of rank are detected by computing the determinant of these matrices and by detecting changes in sign.

The forward and inverse static problems are solved using MATLAB (The Mathworks). We use the MatCont toolbox, which implements the Newton-Raphson method, the continuation algorithm, and the bifurcation detection functions. The integration of the differential equations is performed using the `ode45` function.

C. Experimental setup

The experimental setup used to validate the stability analysis and stiffness modulation strategy presented in the following sections is composed of a motorized TDCR, a shape measurement system, and a tip force generator. The prototype of a planar TDCR is shown in Fig. 2a. It is composed of a tendon-driven manipulator and its actuation unit.

The flexible manipulator is designed so that the assumptions considered in the model are valid. The backbone is composed of two $19\,\mathrm{mm} \times 200\,\mathrm{mm} \times 0.55\,\mathrm{mm}$ leaf springs made of 1075 spring steel (McMaster-Carr), which ensure planar deformations by having a high out-of-plane bending- and torsional stiffness. The two leaf springs are spaced $10\,\mathrm{mm}$ from each other, to avoid collisions with the tendons that run through the centerline between them. The backbone is deformed in a plane by two tendons routed on both sides through rigid spacer disks. The disks are designed to be as light as possible to minimize the effect of gravity on the robot while being able to resist the tendon tension. As shown on Fig. 2b, they are composed of 2 halves fixed on the backbone using M2 screws and are 3D printed using PLA material (Ultimaker B.V, Utrecht, Netherlands). For intermediate spacer disks, the tendon holes are built using two portions of $1.4\,\mathrm{mm}$ diameter NiTi rods, which allow to reinforce the disk and limit the friction with the tendons. The calibrated design parameters of the flexible backbone are given in Table I.

Each tendon is built using two Maxtin 8 cables of $0.17\,\mathrm{mm}$ diameter (KastKing, New York, USA) pulled by two compact DC gear motors (ROB-12285, Sparkfun Electronics, Colorado,

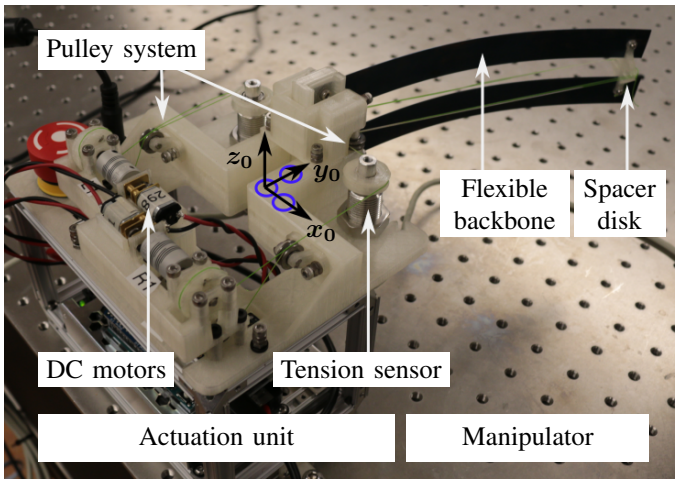

(a) Experimental setup. The robot is composed here of one disk.

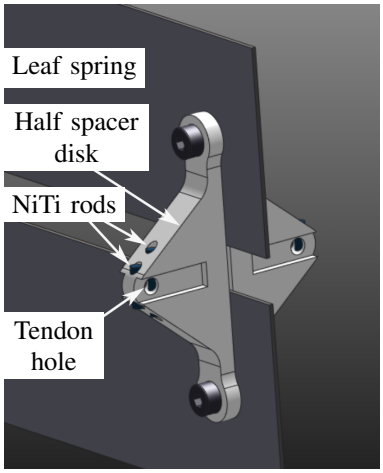

(b) CAD view of a spacer disk.

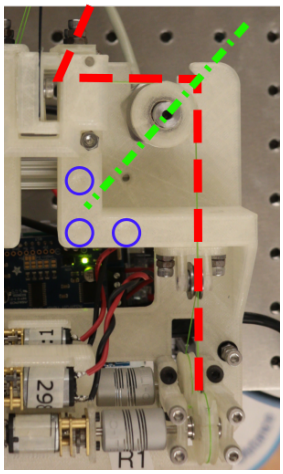

(c) Tendon route in the actuation unit.

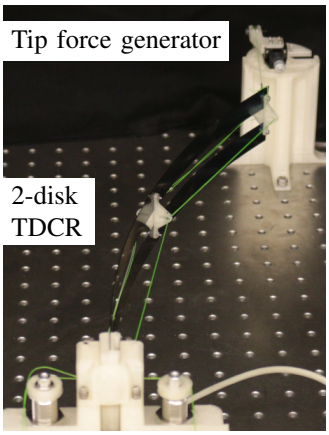

(d) Setup for tip stiffness measurement.

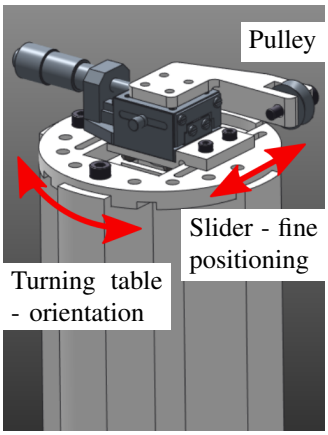

(e) Tip force generator.

Fig. 2: Prototype of TDCR. The tendon route inside the actuation unit is represented in red. The force sensor direction is represented in green. The three indents used to measure the pose of $\mathcal{R}_0$ are indicated with blue circles.

Prototype	L (mm)	r_d (mm)	E (GPa)	I (mm^4)	μ
1 disk	200	13.6	169.52	$5.27e^{-1}$	-
2 disks	400	13	169.52	$5.27e^{-1}$	0.19

TABLE I: Calibrated parameters of the flexible manipulators.

USA) located in the actuation unit. Each motor can exert a maximal tendon tension of $50\,\mathrm{N}$. The tendons are guided in the actuation unit through a set of pulleys, one of them being fixed to a one-degree-of-freedom force sensor RFS100 (Honigmann Industrielle Elektronik GmbH, Wuppertal, Germany) to measure the tendon tension as depicted in Fig. 2c. A PMX amplifier (HBK, USA) is used along with the force sensors, providing a filtered and reliable force measure. Each tendon tension is controlled using a PI controller, implemented on Matlab on a master computer, and calculating a voltage applied to the motors through an Arduino Uno control board equipped with an Adafruit Motor Shield v2 motor driver. The controller gains are empirically determined such that the robot remains stable while accurately reaching the desired tendon tensions. The controller runs at 20Hz with a resolution lower than 0.1N for each tendon, the resolution being limited here by force measurement noises. We assume the force sensor is close enough to the robot base such that the influence of the actuation line stiffness is compensated by the controller in quasi-static regime. The supporting base, the motor pulleys, and the sensor pulleys are 3D printed. They are placed on top of an aluminum frame housing the Arduino board and the power supply.

The robot shape is measured using a laser scanner (FARO Technologies, Florida, USA), as it is contact-free, accurate, and adapted to quasi-static measurements. The generated point cloud is expressed in the base frame $\mathcal{R}_0$, measured using 3 indents (blue circles visible on Fig. 2a), and manually cleaned. The robot shape is finally obtained using the backbone extraction algorithm proposed in [33]. Starting from the robot base, the next node is obtained by selecting the point cloud within a circle of radius L/N centered on the current node and iterating in the direction of the mean position with a segment length of L/N. The points visited in the point cloud are finally removed. The same process is applied until all the N nodes have been found. The repeatability of the shape measurement process was evaluated by measuring 5 times the same shape for different robot configurations. The corresponding nodes in the 5 trials are included in a circle with a maximum radius of $0.3\ \mathrm{mm}$ at the robot tip and a mean radius of $0.1\ \mathrm{mm}$ along the backbone.

The stiffness of the TDCR is measured by applying forces with a specific direction and with increasing magnitude to the robot tip, and by measuring the corresponding tip displacement. The force is generated through the use of a cable evolving in the robot plane and attached to the last spacer disk, see Fig. 2d. The cable is guided through a pulley which redirects it towards the gravity direction. Calibrated weights are then hanged to the cable, generating the tip force $\boldsymbol{F_e}$ with a desired magnitude. The pulley position is manually adjusted using the device presented in Fig. 2e. It can be roughly defined by fixing the device on specific locations on the drilled board and refined using a rail tightened by screws. The pulley position is adjusted after the application of the force so that the force direction remains approximately the same once the robot is deformed. The force direction is measured for each experiment using the FARO arm, by scanning the cable and finding the least square line that passes the closest to the generated point cloud. The tip displacement is obtained by measuring the robot shape with and without the tip force and computing the displacement of the last extracted node.

III. Stability analysis of TDCRs with one disk

The stability analysis of the planar TDCR is carried out in three steps. First, a robot composed of one disk is considered in order to complete the results presented in [14] with insights on the buckling phenomenon and its dependence on design parameters. Second, a stability criterion is formulated for this particular case study. Third, these results are extended to TDCRs composed of multiple disks.

A. Buckling analysis

We consider the case study proposed in [14], where the behavior of a TDCR composed of $n = 1$ disk, moving in free space and actuated by pulling on one of the two tendons is investigated. Numerically, the force applied on tendon 1, T_1, is progressively increased while $T_2 = 0$ N, and the corresponding robot configurations are computed using the continuation process. The computed robot configurations form a bifurcation diagram, which is represented in Fig. 3a along with the corresponding robot shape in Fig. 3b. Pulling on the second tendon, i.e. increasing T_2 while $T_1 = 0$ N, results in a similar bifurcation diagram but mirrored with respect to $\theta(L) = 0$.

We can draw two main observations from these results. First, the bifurcation diagram is composed of two disconnected branches, denoted Branch 1 (configurations 1 to 5) and Branch 2, with Branch 2 being composed of a stable portion (configuration 6) and an unstable one (configuration 7) separated by a LP bifurcation. Consequently, 3 configurations of the robot exist for the same value of $T_1 > 29.3$ N, one of them being elastically unstable. This is consistent with the observations made in [14], where two stable configurations were achieved for the same tendon tension. As a note, the stable portions of the two branches end at a maximum tendon force of $T_1 = 46$ N, for which the tendon hole on the end disk collides with the tendon hole at the robot base (configuration 5). Also, as the two branches are disconnected, the robot cannot pass from Branch 1 to Branch 2 by pulling on one tendon only and without significant tendon length variations. For the design of TDCR considered here, for example, Branch 2 can be reached by pulling first on the second tendon until $T_2 = 32 > 29.3$ N, then by releasing it gradually while increasing T_1 so that at the end $(T_1, T_2) = (32, 0)$ N. Sudden transitions between the two branches can also occur due to external forces, experienced during interactions with the environment for example. To show this, we consider a TDCR with a disk radius of $2\,\mathrm{mm}$ subject to a tip force with an orientation $\phi = -\pi/8$. The tendon tension T_1 is

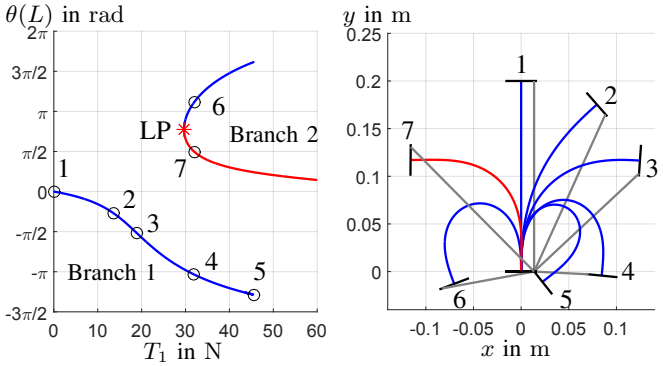

(a) Bifurcation diagram. (b) Robot shapes.

Fig. 3: Stability analysis of a TDCR composed of one disk at the tip and deformed by increasing the tendon tension T_1. Stable and unstable robot configurations are represented in blue and red resp. A Limit Point (LP) bifurcation is detected, indicated by a red star. On the right side, a subset of robot shapes is represented, the actuated tendon being plotted in grey.

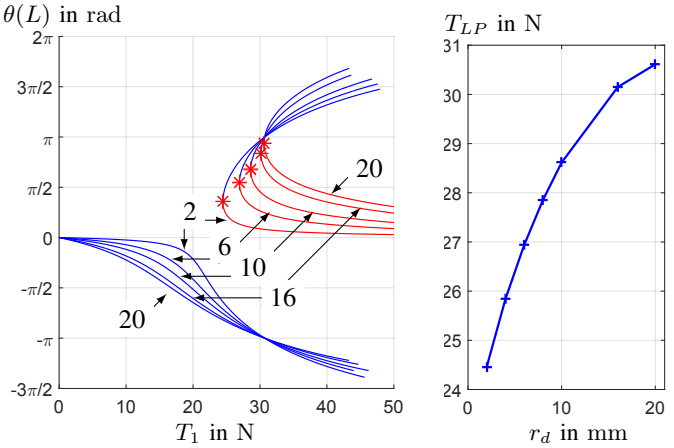

(a) Bifurcation diagram. Red stars indicate LP bifurcations. The values of r_d in mm are written on the graph.

(b) Tendon force at the LP bifurcation.

Fig. 5: Evolution of the bifurcation diagram according to the disk radius.

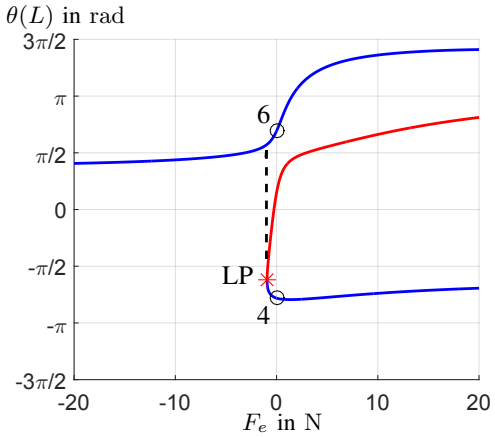

Fig. 4: Stability analysis of a TDCR composed of one disk at the tip, actuated with $T_1 = 32\,\mathrm{N}$ and deformed by increasing the external tip force magnitude F_e. The tip force orientation is $\phi = -\pi/8$ and the disk radius is $r_d = 2\,\mathrm{mm}$. Stable and unstable robot configurations are represented in blue and red resp. A Limit Point (LP) bifurcation is detected, indicated by a red star.

increased above the tension at the LP bifurcation, and the force magnitude is varied with the continuation process. The resulting bifurcation diagram is presented in Fig. 4. Starting from the free space configuration 4, applying a negative force leads to an LP bifurcation, after which the robot jumps on the upper branch as shown by the black dashed line. Reducing F_e to $0\,\mathrm{N}$ afterwards leads to robot configuration 6.

Second, the tendon force beyond which the TDCR can have multiple configurations is marked by the LP bifurcation. The force at which this bifurcation occurs, denoted T_{LP}, depends on the robot design parameters, in particular on the distance r_d between the tendon holes and the backbone as stressed in [14]. To evaluate this, the diagram in Fig 3 is computed for different values of r_d and superimposed on Fig. 5. As r_d increases, the tendon force at the LP increases as well, until it reaches the point where the robot cannot be bent further. This seems consistent, as the larger r_d the more predominant the tendon moment applied on the backbone is compared to the tendon force. As a result, since the buckling phenomena and the LP bifurcation are due to the tendon force, they appear at a higher tendon tension. The tendon force at the LP evolves in a quadratic fashion with r_d as shown in Fig. 5b. This differs from the results in [14], where the relationship is presented as linear. This discrepancy may be due to the difficulty of detecting accurately these cardinality changes using standard numerical solvers. However, their assumption of linear behavior could be considered acceptable, as the curve non-linearity is not significant.

B. *Stability criterion*

A global stability criterion gives a lower bound of the actuation values leading to stability losses as a function of the robot design parameters, typically without considering external forces applied on the robot [7]. Finding the analytical expression of the force at the LP bifurcation would provide such a relation. However, this task is complex because of the non-trivial shape of the robot in this configuration. Instead, we propose to find a criterion by making parallels with existing beam buckling problems.

According to Eq.(3), a single disk TDCR is subject to two different wrenches at its tip: a tendon force, which is parallel to $\overrightarrow{O_0O_1}$ due to the straight tendon routing, and a tendon moment. Considering the effect of the force only, the backbone is in a buckling configuration identical to the guyed beam studied in [34] when the cable is attached at the beam base. As the tension in the cable increases, the beam is compressed and stays in a straight trivial configuration until buckling occurs, resulting in a super-critical pitchfork behavior. This scenario is investigated for the 1-disk TDCR using the continuation method by fixing $T_1 = T_2 = T_t/2$ and

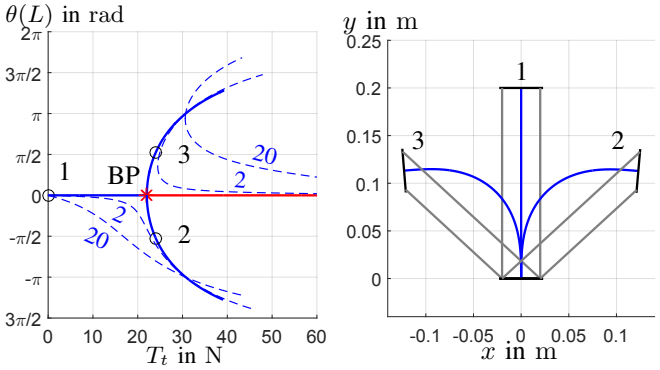

(a) Bifurcation diagram. (b) Robot shapes.

Fig. 6: Stability analysis of a TDCR composed of one disk at the tip and deformed by pulling on the two tendons simultaneously with a total force T_t. Stable and unstable robot configurations are represented in blue and red resp. A Branch Point (BP) bifurcation is detected, indicated by a red star. The bifurcation diagrams obtained by pulling on tendon 1 with r_d =2 mm and r_d =20 mm are presented with dashed lines. The values of r_d are indicated in blue. On the right side, a subset of robot shapes are represented, the actuated tendon being plotted in grey.

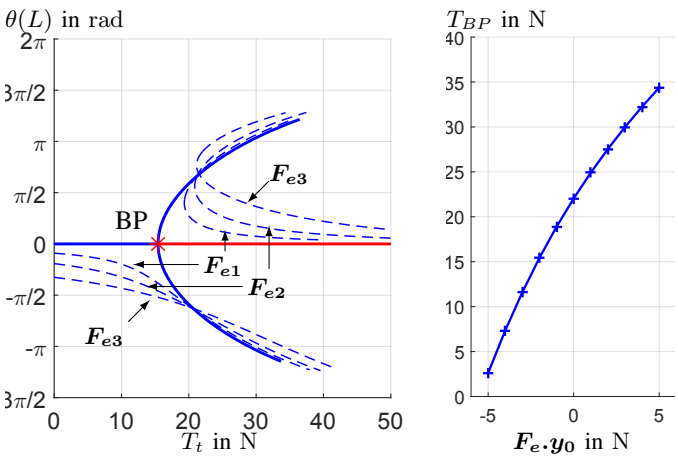

(a) Bifurcation diagrams considering different tip forces $\boldsymbol{F_e}$: (F_e, ϕ): plain line $\boldsymbol{F_e} = (2, \pi/2)$, and dashed lines $\boldsymbol{F_{e1}} = (2.16, 5\pi/8)$, $\boldsymbol{F_{e2}} = (2.83, 3\pi/4)$, $\boldsymbol{F_{e3}} = (5.23, 7\pi/8)$

(b) Tendon force at the BP bifurcation.

Fig. 7: Evolution of the bifurcation diagram according to the external tip force.

by varying the total force T_t applied on the backbone. The resulting pitchfork bifurcation diagram is shown in Fig. 6. The robot remains straight until a critical tendon force indicated by a BP bifurcation, denoted T_{BP}, beyond which two stable and one unstable configurations exist. The critical tendon force corresponds to the buckling force of a hinged-hinged cantilever beam, as explained in [34]. By linearizing the static model around the straight robot configuration, we can obtain the relation between the critical tendon force and the design parameters:

$$T_{BP} = \frac{EI\pi^2}{L^2} \tag{12}$$

For our prototype, the stability criterion results in T_{BP} = 22.04 N, which corresponds to the value of tendon tension at the BP bifurcation on Fig. 6. The stable branches stop at the tendon tension 39 N, under which the tendon holes at the end-disk and the base coincide. The unstable branch continues on with $T_t \to \infty$.

It is well known that the force at the critical pitchfork bifurcation obtained in the trivial straight configuration is a lower bound of the tendon forces beyond which stability issues can occur when perturbations are applied on the beam. The tendon moment acts as such a perturbation. To illustrate this, the diagrams obtained when pulling on one tendon are plotted with dashed lines on Fig. 6 for r_d =20 mm and r_d =2 mm. In this case, the total tendon force is applied on tendon 1, resulting in $T_t = T_1$. We can see that the lower the value of r_d, the lower the tendon moment and the closer the bifurcation diagram is to the pitchfork diagram. We observe also that $T_{BP} < T_{LP}, \forall r_d$ as expected.

The same strategy can be applied to analyze the effect of an external tip force $\boldsymbol{F_e}$ on the TDCR elastic stability. One can construct a similar super-critical pitchfork behavior by considering a tip force aligned with the backbone axis at rest, $\pm\boldsymbol{y_0}$ in our case. The bifurcation diagram obtained by pulling on the two tendons with F_e =2 N and $\phi = \pi/2$ is shown on Fig 7a. A similar pitchfork diagram is obtained, with a critical tendon force T_{BP} =15.43 N. As before, this tendon force marks a stability limit of the TDCR under perturbations. Changing the orientation of the tip force will create additional bending moments along the backbone and create such perturbations. To illustrate this, we superimpose the diagram obtained by pulling on the two tendons but with different tip forces on Fig 7a. The tip forces have different orientations but equal components along $\boldsymbol{y_0}$. As expected, we obtain that $T_{BP} < T_{LP}, \forall \boldsymbol{F_e}$. The value of T_{BP} depends on $\boldsymbol{F_e}.\boldsymbol{y_0}$, which we investigate by evaluating numerically the critical tendon force for different tip force magnitude with $\phi = \pi/2$. The results are presented in Fig 7b. As the tip force magnitude increases in the $-\boldsymbol{y_0}$ direction, T_{BP} decreases and reaches 0 for F_e =5.5 N. This value of F_e is the critical tip force that provokes buckling without any tendon tension. It corresponds to the buckling force of a fixed-hinged cantilever which is written $F_e = EI(\pi/(2L))^2$. On the contrary, applying a tip force along $\boldsymbol{y_0}$ increases significantly the value of T_{BP} and thus stabilizes the robot.

To summarize, we identified here a global stability criterion for a TDCR with one disk: the maximum tendon force until which the robot is stable given its design parameters. This criterion can be used to design stable robots, where the maximum tendon force is imposed and the backbone parameters are chosen accordingly, or to ensure elastic stability during control, where the backbone parameters are fixed and the tendon tension varies. It also indicates the level of pre-tension that can be applied to the tendons without inducing buckling effects.

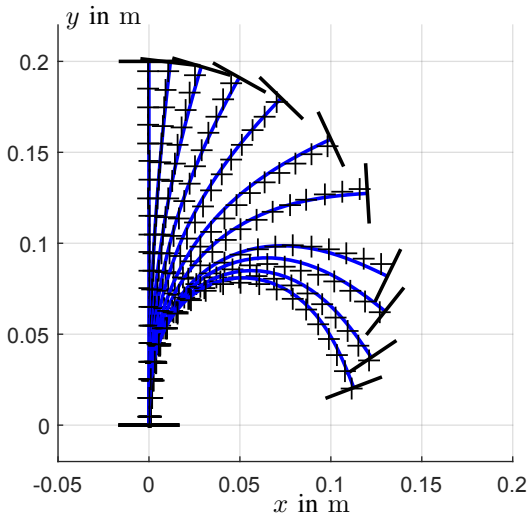

Fig. 8: Comparison between measured and calculated shapes for the 1-disk prototype of TDCR. The measured nodes are depicted with black crosses. Only 20 of them are represented for clarity. The robot backbone predicted by the static model is depicted with solid blue lines.

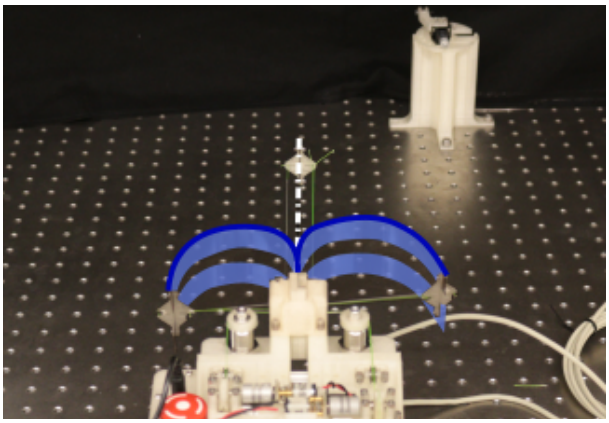

Fig. 9: Stable robot shapes obtained for a robot with 1 spacer disk. The two bent configurations are highlighted with solid blue curves. The leaf springs composing the backbones are colored light blue. The initial straight configuration is highlighted with a dash-dotted white line.

C. Experimental validation

The static model is assessed for the case of the 1-disk TDCR deformed by pulling on tendon 1 only. A set of 11 different values of tendon tension equidistributed in the range $[0\,\mathrm{N}, 27\,\mathrm{N}]$ were applied. For each value, we measured the robot shape once the robot converged to a steady state. For the shape reconstruction from the point cloud, the backbone is discretized in $N = 40$ nodes. The backbone Young modulus E and the disk radius r_d are then calibrated from the experimental data to account for material property variability and assembly tolerances. They are estimated so that the mean error between the measured and calculated robot tip positions for all the tested configurations is minimized. The minimization is performed with a Levenberg-Marquardt algorithm implemented in the `fminsearch` MATLAB function. The values of the calibrated parameters are listed in Table I. The computed and measured robot configurations are represented on Fig 8. The results show a good correlation between the model and the experiments, with a tip position error of 2.90 ± 1.40 mm, which represents 1.45% of the robot length. The shape error, which is computed for each configuration as the mean position error over the nodes, is 1.70 ± 0.86 mm or 0.85% of the robot length. The tip orientation error is calculated by comparing the value of $\theta(L)$ given by the model to the experimental orientation. The latter is obtained by computing the slope of the least square straight line passing through the last five nodes at the tip. The orientation error is $2.45 \pm 2.02°$. This validates the ability of the model to predict the backbone shapes obtained during tendon actuation.

We also observe experimentally the non-trivial robot shape that belongs to the secondary branch in Fig. 3, visible on the left side of Fig. 9. The configuration is obtained by manually pre-bending the robot in the $-\boldsymbol{x_0}$ direction and then applying a tendon tension above the value at the LP bifurcation T_{LP}. The robot then converged towards the expected bent configuration in the direction $-\boldsymbol{x_0}$.

IV. Extension to TDCRs with n disks

A. Buckling analysis

The results presented before can be extended to planar TDCRs composed of n disks. They are generated using our numerical approach for different values of n while conserving the same arc length between two disks by setting the robot length at $L = nL_d$ with $L_d = 200$ mm. We assume initially that friction is negligible to ease the interpretation of the results. This assumption is relaxed later.

Pulling on one tendon leads to a more complex bifurcation diagram composed of four disconnected branches of equilibrium configurations, denoted Branch 1 to 4, as shown on Fig. 10a. A selection of robot configurations picked on these branches are represented on Fig.10b. Branch 1 and 2 are similar to the ones observed for $n = 1$. Their stable portions are characterized by robot configurations where the two subsegments have a similar curvature which is either negative (configuration 1 to 5) or positive (configuration 6). Branch 3 and Branch 4 are also partially composed of stable robot configurations, but which form S-shapes (configuration 8,9). The curvature has the same sign along each subsegment and opposite signs between the two subsegments. Both extremities of Branch 4 extend to $T_1 \to \infty$. As a summary, we find 9 different configurations of the 2-disks TDCR for the same value of $T_1 > 30$N. Four of the configurations are evaluated as stable (configuration 5,6,8,9). They are characterized by robot shapes where the variations of curvature, along one subsegment or between the two subsegments, are minimal. This is consistent with the fact that a stable configuration is a minimum of the robot potential energy.

B. Stability criterion

Pulling on the two tendons simultaneously leads to the bifurcation diagram shown in Fig. 11, which is composed

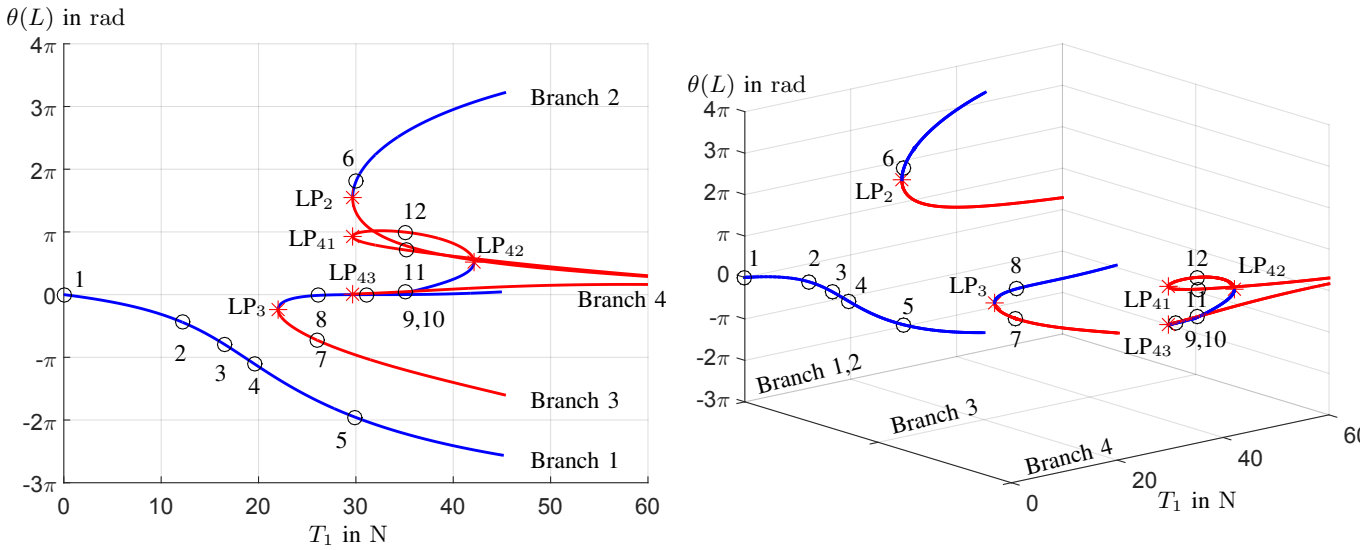

(a) Bifurcation diagram.

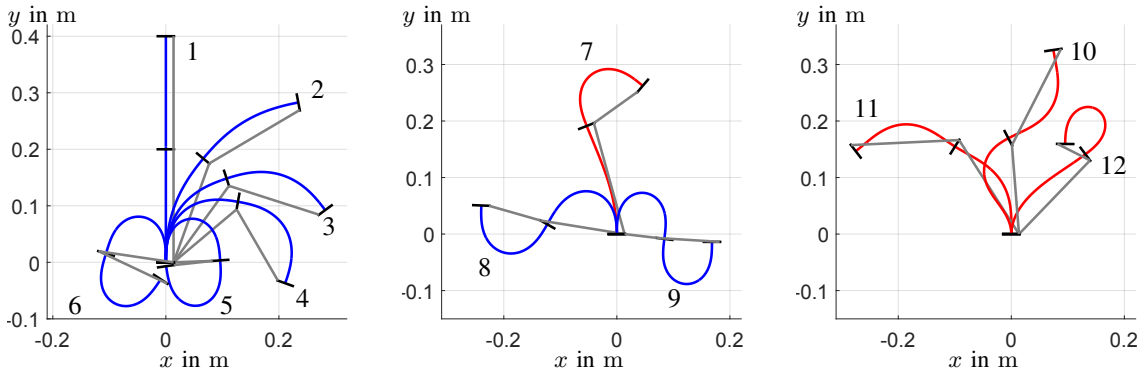

(b) Robot shapes.

Fig. 10: Stability analysis of a TDCR composed of two disks and deformed by increasing the tendon tension T_1. Stable and unstable robot configurations are represented in blue and red resp. Limit Point (LP) bifurcations are detected, indicated by a red stars. On the right side, a subset of robot shapes are represented, the actuated tendon being plotted in grey.

of 5 branches. Branches 1 and 2 are composed of robot configurations where the backbone curvature is zero (configuration 1) or has the same sign along the two subsegments (configuration 2 and 3), similar to the case where $n = 1$. They intersect at a BP bifurcation located at $T_{BP} = 22.04$ N. Branch 3 and 4 are composed of robot configurations where one of the subsegments is straight and the other is bent. This can be interpreted as the straight subsegment staying in the trivial configuration while the other one is buckled. They are evaluated as unstable, which is to be expected as one of the subsegments is in a straight, unbuckled configuration even after the critical tendon force. Finally, Branch 5 is composed of stable robot configurations where the backbone experiences a S-shape (configurations 8 and 9). Along this branch, the tip orientation is constant and equal to $\theta(L) = 0$ rad. As a summary, when pulling on both tendons, the TDCR can have 9 different configurations for the same tendon tension. The robot shapes shown in Fig. 11 are obtained with the same total tendon force of $T_t = 25$N.

We can also observe from Fig. 11 that T_{BP} is the same as the one obtained from $n = 1$. This is likely to be due to the subsegment length L_d which is the same for the two cases. Moreover, we saw that some robot configurations obtained after the bifurcation have only one buckled subsegment. These observations hold when using more subsegments. To verify this, we compute the bifurcation diagram numerically with the two tendons pulled for numbers of disks going from $n = 3$ to $n = 10$ and the same subsegment length $L_d = 200$mm. For a given backbone stiffness, varying the number of disks while conserving the same inter-disk arc length leads to the same critical force $T_{BP} = 22.04$ N. Assuming that this property holds for $n > 10$, we deduce that the global stability of a TDCR composed of n disks is actually dictated by the global stability of one subsegment, whose length is L/n. Consequently, the global stability criterion can be obtained from Eq. (12):

$$T_{BP} = \frac{EI\pi^2}{(L/n)^2} \tag{13}$$

This criterion can be useful for TDCR design and control, as explained previously, and applies to robot prototypes with any backbone properties and number of disks.

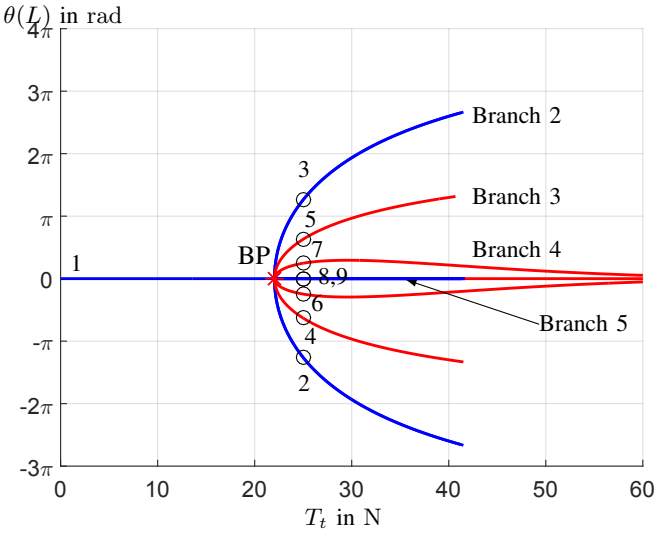

(a) Bifurcation diagram. Red stars indicate limit point (LP) bifurcations.

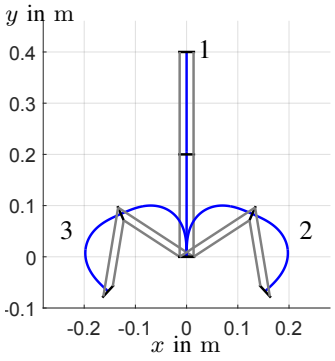

(b) Robot shapes for configurations 1 to 6.

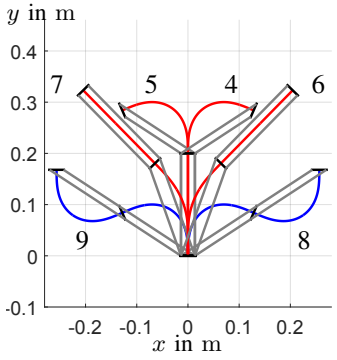

(c) Robot shapes for configurations 7 to 12.

Fig. 11: Stability analysis of a TDCR composed of two disks and deformed by pulling on the two tendons simultaneously with a total force T_t. Stable and unstable robot configurations are represented in blue and red resp. A Branch Point (BP) bifurcation is detected, indicated by a red star. On the right side, a subset of robot shapes obtained for $T_t = 25\,\mathrm{N}$ are represented, the actuated tendon being plotted in grey.

Concerning the impact of an external tip force on the critical tendon force, the same tendency is observed as for the case $n = 1$. For increasing magnitude of $\boldsymbol{F_e}$ in the $-\boldsymbol{y_0}$ direction, T_{BP} decreases in quasi linear fashion until reaching 0 N for $F_e = EI(\pi/(2L))^2$.

Finally, we study the influence of friction between the tendons and the disks on the robot's elastic stability. In particular, we focus on the evolution of the tendon tensions at LP and BP bifurcations with the friction coefficient μ. A complete analysis of the influence of friction on the equilibrium branches is out of the scope of this paper. To study the evolution of T_{LP}, we generate Branches 1 and 2 in the case where one tendon only is pulled (Figure 10) with different values of μ. Reaching the configurations along these two branches does not imply the same direction of tendon motion. The tendon is shortened to bend the backbone in the clockwise direction (Branch 1), and released to bend in the anti-clockwise direction (Branch 2). To account for this phenomenon, we consider a positive and negative value of μ respectively with the same magnitude $\|\mu\|$. The resulting branches are superimposed to the original frictionless diagram in Fig. 12a, and the evolution of T_{LP} with μ is shown in Fig. 12b. We observe that the higher the friction the lower the robot's deformation is, as expected. Also, the value of T_{LP} increases with μ in a quasi-linear fashion. To observe the evolution of T_{BP}, we pull simultaneously the two tendons starting from the undeformed and straight robot configuration, which corresponds to Branch 1 in Fig. 11 for the same values of $\|\mu\|$. We don't observe any change in the critical tendon force. This is to be expected, as in the straight configuration the vectors $\boldsymbol{a_k}$ and $\boldsymbol{x_{b,k}}$ are orthogonal and the friction force is null.

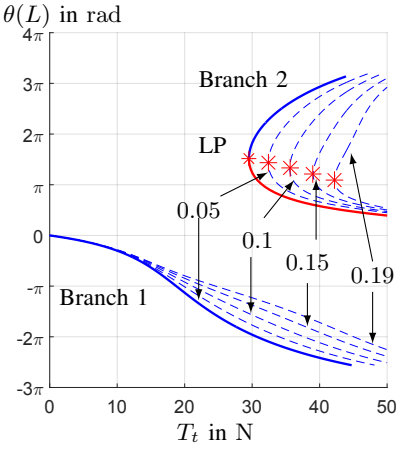

(a) Bifurcation diagrams considering different values of $\|\mu\|$, written on the graph. Solid lines: diagram without friction.

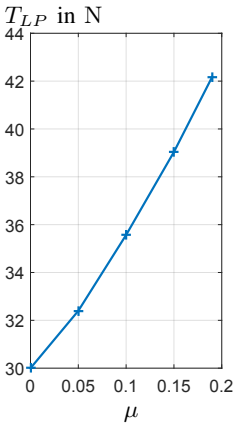

(b) Tendon force at the LP bifurcation.

Fig. 12: Evolution of the bifurcation diagram according to the friction coefficient in the case of a 2-disks TDCR with one actuated tendon.

C. Experimental validation

We use the same process to validate the static model in the case of the 2-disk TDCR. A set of 7 different values of tendon tension equidistributed in the range [0 N,18 N] were applied on tendon 1. To reconstruct the robot shape, each subsegment is discretized with 40 nodes, giving a total of 80 nodes. The value of the friction coefficient between the intermediate disk and the tendon is calibrated to minimize the tip position error. The Young's modulus and disk radius are considered the same as for the 1 disk prototype. The computed and measured robot configurations are represented in Fig 13. Again, the results show a good correlation between the model and the experiments, with tip and shape position errors of 7.2 mm and 4.1 mm respectively, corresponding to 1.8% and 1.02% of the robot length. The tip orientation error is $3.05 \pm 2.01°$. This validates the ability of the model to account for the tendon forces applied on intermediate spacer disks, and the friction forces at the tendon holes.

We finally evaluate experimentally the stability criterion for n disks by trying to reach the different robot configurations

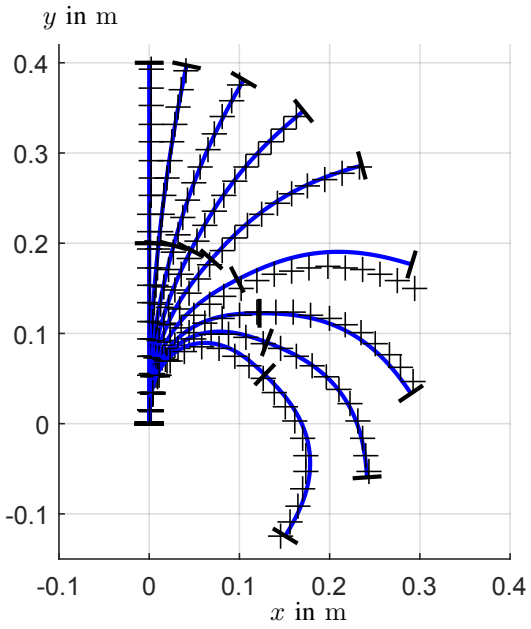

Fig. 13: Comparison between measured and calculated shapes for the 2-disks prototype of TDCR. The measured nodes are depicted with black crosses. Only 20 of them are represented for clarity. The robot backbone predicted by the static model is depicted with solid blue lines.

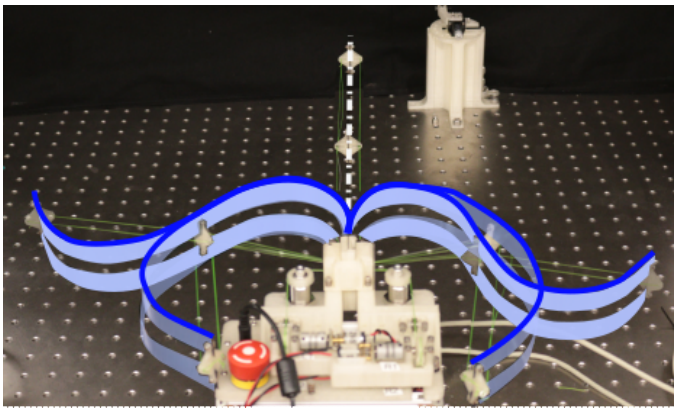

Fig. 14: Stable robot shapes obtained for a robot with 2 spacer disk. The initial straight configuration is highlighted with a dash-dotted white line, and the four bent configurations with curvature having the same sign (C-shape) or opposite sign (S-shape) along the subsegments with solid blue curves.

presented in Fig. 10. As previously, the robot is manually pre-deformed in the targeted shape and the control is run until an equilibrium is reached. We obtain the four stable configurations depicted on Fig. 14. As expected, we obtain two configurations where the backbone curvature has the same sign along the two subsegments and two others that exhibit an S-shape.

V. Application: Active Softening

In this section, we present the concept of buckling-based active softening considering the straight buckling configuration described in Sec.IV-B. We propose an open-loop strategy to control the tip orientation and the robot stiffness simultaneously. Finally, the control strategy is validated experimentally.

A. Principle of buckling-based active softening for TDCR

To illustrate the impact of buckling on the TDCR stiffness, we consider the case where the robot is composed of two disks, the backbone is initially straight, and the two tendons are pulled simultaneously. This case scenario is depicted in Fig. 15a. In this configuration, the total tendon force applied on the flexible backbone can be increased up to the critical tendon force without altering the robot shape by applying the same tension on the two tendons. When an external force is exerted at the tip, the robot deforms, and the tendons' configuration changes. The tendon force produces interaction forces on the disks, depicted with grey arrows in the figure, that favor the robot bending. As a result, when the tendon force increases, the backbone experiences larger deflections for the same external force at the tip and the robot stiffness is lower. We show that phenomenon numerically by applying tip forces with orientation angles $\phi = 0$ rad and $\phi = -\pi/2$ rad and of small magnitude $\|\boldsymbol{F_e}\| = 1e^{-6}$ N on the robot. The tendon force is then progressively increased and the tip displacement in the force direction Δx (resp. Δy) is observed. The robot stiffness K_{xx} (resp. K_{yy}) with respect to the tip force is finally computed as $K_{xx} = \boldsymbol{F_e^T x_0}/\Delta x$ (resp. $K_{yy} = \boldsymbol{F_e^T y_0}/\Delta y$). The results are shown in Fig 15b. As the tendon force increases, the TDCR can no longer support the constant but small load it experiences and undergoes a large displacement. As a result, the TDCR stiffness reaches nearly $0\,\mathrm{N/m}$ at the critical tendon force. Beyond this tendon force, the robot configuration is unstable, leading to a negative stiffness typical of zero-stiffness compliant mechanisms [24]. A negative stiffness means here that the robot internal forces, which comprise the elastic and tendon forces, do not oppose the deformations induced by the tip force as they normally do but favor them. As a consequence, the robot continues moving until it reaches a post-buckling stable configuration, such as configurations 2, 3, 8 and 9 in Fig. 11.

As a conclusion, tendon actuation can be used to obtain large variations of the robot stiffness. Buckling-based active softening with tendon actuation provides an alternative to existing variable stiffness technologies without adding components to integrate into the backbone. Therefore, a smaller footprint can be achieved while having the advantages of tendon actuation, such as easier continuous control and potentially higher dynamics.

B. Open-loop control of tip orientation and stiffness

Using the principle of buckling-based active softening, we propose an open-loop control strategy for planar TDCR where the tip orientation $\theta(L)$ and the robot global stiffness are controlled simultaneously. The actuation inputs to apply to the robot are computed using the inverse static model to obtain a desired tip orientation θ_d. We also impose a desired tendon force T_d applied on the backbone to bring the robot closer to or farther from its stability limit. In order to validate this control

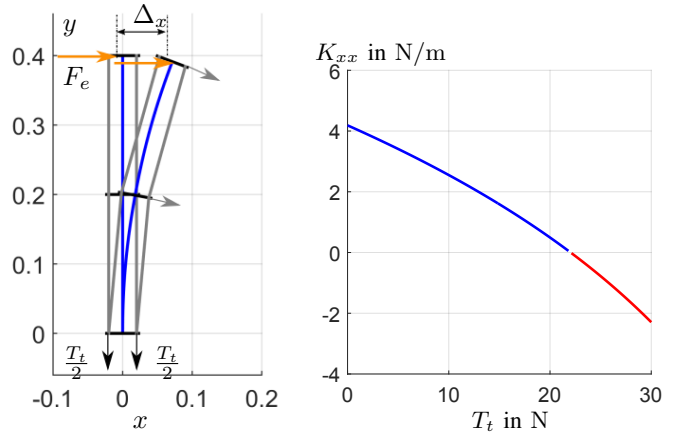

(a) Schematics of applied forces.

(b) Evolution of S_x with respect to the tendon force.

Fig. 15: Demonstration of the buckling-based active softening of TDCR, in the configuration where the robot is straight and the same force is applied on both tendons. The blue and red curves on the right represent stable and unstable configurations respectively.

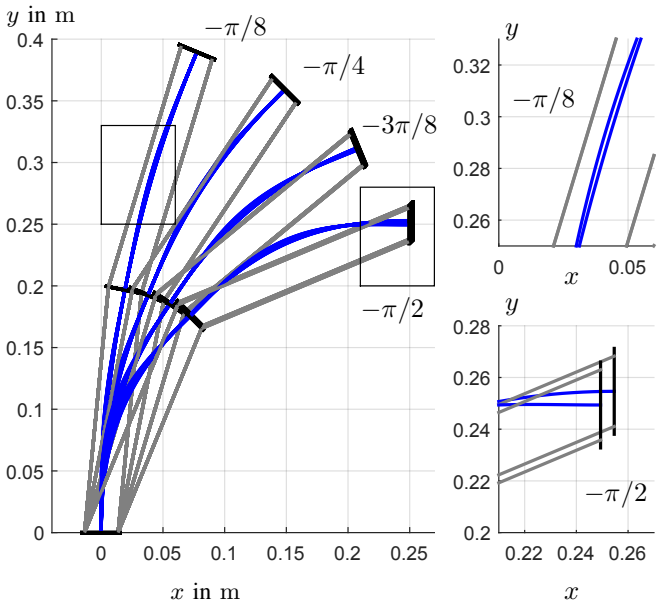

(a) Robot shapes. On the zoomed figures, only the most different configurations obtained with the lowest and highest tendon force are represented for $\theta_d = -\pi/4$ and $\theta_d = -\pi/2$.

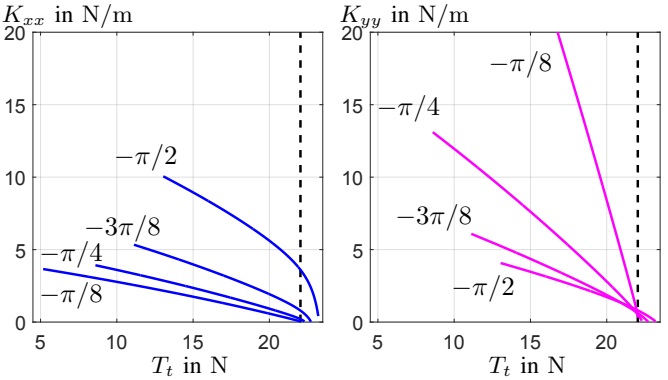

(b) Evolution of S_x with respect to the tendon force.

(c) Evolution of S_y with respect to the tendon force.

Fig. 16: Demonstration of the buckling-based active softening of TDCR for non-straight configurations. The values of θ_d in rad are written on the graphs. T_{BP} is indicated with a black dashed line.

strategy numerically, the inverse static problem is solved for several values of θ_d. For each tip orientation, T_d is increased to the critical tendon force. We neglect the effect of friction between the tendons and the disks to ease the convergence of the inverse static model.

The resulting robot shapes and robot stiffness are presented in Fig. 16. In Fig. 16a, the robot shapes obtained for the different values of θ_d and T_d are superimposed. The zoomed views show the most different configurations for $\theta_d = -\pi/8$ and $\theta_d = -\pi/2$. First of all, we observe that we can successfully reach a given bending angle with different values of total tendon force. The inverse static model converges, and the error in tip orientation is zero modulo the solver tolerances. We also observe that there are small variations between the robot shapes for a given value of θ_d. This property is likely due to the TDCR construction, in particular to the fact that the two tendons terminate at the same spacer disk (the backbone tip) and their routing is symmetric with respect to the robot backbone. The shape differences, which is the mean distance between corresponding nodes in the two configurations, are 1.10 mm and 5.20 mm respectively, i.e. $0,28\%$ and $1,30\%$ of the backbone length. These variations are similar to the position accuracy of standard static models of TDCR [29], [35]. Consequently, without having implemented a specific position controller, we can vary the total tendon force while maintaining the segment shape, with variations that could be experienced with state-of-the-art model-based planners or open-loop position control schemes.

The variations of robot stiffness obtained for each value of θ_d are shown in Fig. 16b and Fig. 16c. Only the stiffness values corresponding to stable robot configurations are depicted. The different curves do not start at the same value of T_t, since the minimum tendon force required to reach θ_d increases with it. As previously, we observe a quasi-linear decrease of K_{xx} and K_{yy} with respect to the total tendon force, until it eventually reaches $0\,\mathrm{N/m}$. While the stiffness becomes null at T_{BP} for $\theta_d = -\pi/8$ and $\theta_d = -\pi/4$, stable configurations beyond the critical tendon force are computed for the two last tip orientations. In particular, the total force at which the stiffness becomes zero increases with θ_d. This is due to the boundary condition (7) we added to the system to solve the inverse static problem, which constrains the robot tip orientation to stay at the desired value. In conclusion, the robot tip stiffness can be theoretically decreased to zero without altering the robot tip orientation and with small variations of the robot shape. This validates the effectiveness of the proposed open loop control as a buckling-based active softening strategy.

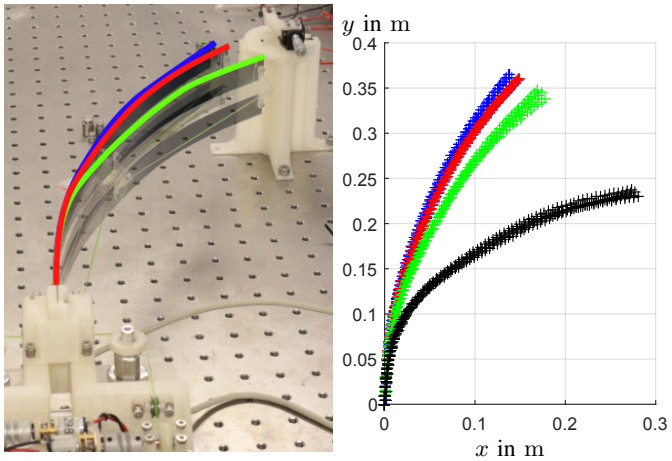

(a) Overlay of robot configurations. (b) Measured backbone position.

Fig. 17: TDCR shape in free space obtained after applying the tendon forces calculated with the inverse model for $\theta_d = -\pi/4$ and $T_t = \{8.6, 13.0, 17.0\}$ N. The robot shapes are depicted in blue, red and green for each total force respectively. The robot shapes obtained for $T_t = 21.0$ N are depicted in black.

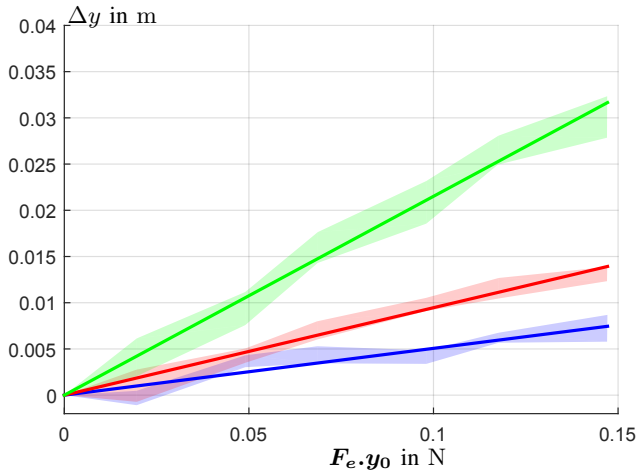

Fig. 18: Displacement to tip force relation for different values of total tendon force applied on the backbone and for $\theta(L) = -\pi/4$. The distributions of the measured values for each tip force amongst the 5 trials are represented with blue, red, and green areas. Plain thick lines represent the linearized relationship.

C. Experimental validation

We validate the active softening strategy experimentally for $\theta_d = -\pi/4$ and for tip forces in the $\boldsymbol{y_0}$ direction. The tendon forces computed with the inverse static model are applied to the prototype for four different values of total tendon force: $T_t = 8.6$ N and $T_t = 21.0$ N, which correspond to the minimum force required to reach $\theta(L) = \pi/4$ and the force just before the stability limit respectively, and 2 intermediate forces $T_t = 13.0$ N and $T_t = 17.0$ N. For each value of total force, the tip stiffness is estimated by applying tip forces with increasing magnitude and measuring the corresponding robot shape and tip displacement. The different force magnitudes are obtained with a set of calibrated weights of mass $\{2, 5, 7, 10, 12, 15\}$ g. Each robot configuration is established 5 times, returning to the straight robot configuration between each trial.

The robot shapes in free space obtained for the 4 total forces are represented in Fig. 17. We can see that for $T_t = \{8.6, 13.0, 17.0\}$ N, the computed tendon tensions lead to similar robot shapes. The tip orientation errors are $8.76 \pm 1.41°$, $7.60 \pm 0.19°$ and $2.34 \pm 3.39°$ respectively, resulting in a mean tip orientation variation over the different values of T_t of $6.42°$. These values seem acceptable considering that friction was neglected and the accuracy of the open loop control is limited to the static model accuracy. Indeed, the orientation variation is similar to the tip orientation error reported in section IV.C, which was obtained by accounting for friction. We observe an error of $25.02 \pm 2.52°$ for $T_t = 21$ N. This is expected, as the robot becomes more sensitive to small perturbations when getting closer to the stability limit. Due to this error, interpreting the change of stiffness would be difficult since it would be due to the change in total force but also the change in robot shape. Therefore, we measure the tip stiffness for the three first values of total force only.

The tip displacements along $\boldsymbol{y_0}$ obtained after application of the calibrated weights are depicted in Fig. 18. The maximum and minimum values amongst the 5 trials are indicated by thin plain lines, the colors corresponding to the different values of T_t. Linear regression is performed on all the measures related to a given T_t. The offset from the obtained linear relationship is deducted from the data points and the fitted lines in Fig. 18. The slope of the line gives the compliance at the robot tip along $\boldsymbol{y_0}$ $K_{yy}^{-1} = \Delta y/(\boldsymbol{F_e^T y_0})$, from which the stiffness can be deduced. For $T_t = \{8.6, 13.0, 17.0\}$ N, we obtain $K_{yy} = \{19.75, 10.67, 4.65\}$ N/m. As expected, the total tendon force has a significant impact on the stiffness at the tip of the robot. The value of K_{yy} is approximately divided by 4 when passing from $T_t = 8.6$ N to $T_t = 17.0$ N, i.e. when doubling the total force. Also, the stiffness can be varied continuously on this range by changing the value of T_t. The measured values of stiffness show some discrepancies with the values predicted by the model in Fig. 16c. For the same values of total force, the stiffness values predicted by the model are $K_{yy} = \{13.10, 9.41, 5.74\}$ N/m, resulting in errors of $\{50.76\%, 13.39\%, 18.90\%\}$ of the theoretical values. This is attributed to the fact that the tip force magnitude in simulation is much lower than in experiments. In order to measure the stiffness, high-enough tip forces had to be applied in order to observe distinct tendon tension variations during control, and therefore to obtain distinct tip displacement. As a result, larger changes in configurations are obtained, which are impacted by the non-linearity of the robot behavior. Nevertheless, this experiment demonstrates the effectiveness of the buckling-based active softening strategy.

VI. Discussion

The results obtained during the stability analysis improve the understanding of the behaviour of TDCR. They give useful

insights on how to design and control these robots, such as what pre-tension can be applied on the tendons without inducing buckling, or what are the different configurations the backbone can achieve for a given set of tendon tensions. The buckling-based stiffness modulation strategy also reveals to be effective in reducing the robot tip stiffness significantly. In this section, we discuss some other ways of using these results in practice, as well as some limitations of this work. In particular, our numerical results depend on the assumptions we considered in the static model, which are discussed below.

A. Assumption 1: Absence of backbone self-collisions

Some results of the stability analysis depend on the assumption that the tendons cannot collide with the backbone, or that the backbone cannot collide with itself. In particular, the non-trivial robot shapes presented in Fig. 3 and 10, all the configurations of the trivial branches above $F_1 = 31\text{N}$ on Fig. 10, and the non straight configurations of Fig. 6 will be affected by these collisions. These configurations might be altered or might not exist for standard designs of TDCR where the backbone consists of a standard tube or leaf spring. However, several results still apply to these designs. The value T_{BP} will be the same, as the backbone is not subject to any self-collision when reaching the critical tendon force. The backbone is also free to achieve small bending around the straight configurations beyond T_{BP}. The stiffness modulation strategy is applicable to standard TDCR designs. As shown in Fig. 16, the robot configurations obtained with $\theta_d = -\pi/8$ do not present collisions between the tendons and the backbone, while the stiffness still decreases towards 0 N/m while increasing the total tendon force. By considering a backbone composed of more disks, which is often the case in the literature, larger collision-free values of θ_d can be achieved. We also think that the interesting shapes obtained beyond the critical tendon force can motivate new designs of TDCR. Indeed, achieving different shapes with continuum robots without adding actuators, such as the S-shapes we present in Sec.IV, is an active research topic [36], [37].

B. Assumption 2: Tendon force control

The results presented in this work are valid for TDCR where the tendon tension is controlled rather than the tendon displacement. This is important to notice, since switching between these two actuation modalities can result in significant changes of behaviour as demonstrated in [38]. In particular, the authors in this work showed that the pre-tension of the tendons has no effect on the robot stiffness when the tendon is fully constrained along the backbone and its displacement is prescribed. As a result, the effectiveness of the stiffness modulation strategy we propose shows the interest of using tendon tension control for TDCR.

From an application point of view, this tension control requires a tension sensor that cannot always be placed at the backbone base, especially in medical applications where small form factors are important. In that case, the sensor might be deported farther from the backbone base, requiring to consider the actuation line stiffness in the static model as considered in previous works. Alternatively, the research community of cable-driven mechanisms has developed a number of compact solutions for tension sensing, including small-scale compliant bodies equipped with strain gauges [39], [40] and self-sensing tendons composed of multiple resistive fibers [41], that could be integrated close to the backbone base.

C. Assumption 3: Planar robots composed of spacer disks

The results of the stability analysis and the stiffness modulation are valid for planar TDCR composed of spacer disks. Therefore, they apply directly to several existing designs of TDCR, where the robot deformations have been restricted to a plane to facilitate design and control. It is interesting to note that, as the number of disks contributes quadratically to the critical tendon force, this force increases rapidly with n for a given robot length. As a result, the larger the number of disks, the larger the actuation space where the TDCR stays elastically stable. Also, the critical tendon force may become larger than the force that can sustain the tendon without breaking. In that case, the considered TDCR cannot become unstable, but loses also interesting features such as the configuration multiplicity and the stiffness modulation. This could motivate the use of new materials for the tendons, that can resist higher magnitudes of tendon tension. To push this topic further, the critical tendon force approaches infinity when the number of disks does, this last case being equivalent to having tendons fully-constrained along the backbone [28]. Fully-constrained tendons are usually realized by continuously guiding the tendons along the backbone through lumens, and can lead to a significantly different behaviour. As a result, TDCR with fully-constrained tendons might theoretically not be subject to any buckling phenomenon. They might be elastically stable for any tendon tension, but, again, at the cost stiffness modulation and shape changing abilities. However, in practice, TDCR with tendons guided through channels might still be subject to buckling. Buckling could occur due to errors in the planar restriction, the mechanical play between the tendons and the channel and imperfect robot fabrication and assembly. A deeper analysis of the effect of these imperfections on the TDCR stability is definitively of interest for predicting buckling phenomena more accurately and using them.

VII. Conclusion

In this work, we present an extensive stability analysis of planar TDCR composed of spacer disks for the first time, based on both numerical analyses and experimental assessments. We show that TDCRs can have multiple configurations for the same actuation inputs, confirming and completing existing results on the 1-disk robot and extending them to two disks. The unstable configurations can lead to sudden changes of configuration eventually which are to be avoided in sensitive environments. The stable ones present interesting shapes, such as S-shape curves, that could be exploited to obtain different kinematic properties. We also show that these configurations appear when the total tendon force applied on the robot backbone goes beyond a critical value, which depends on the backbone design parameters. We provide an

analytical expression of this critical tendon force, which can be used to design stable TDCR, determine the pre-tension to apply on the tendons or to ensure the robot elastic stability during control. Finally, we show that this buckling behavior can be leveraged to decrease the robot stiffness with small alteration of its shape. The robot stiffness can in theory be reduced down to quasi $0\mathrm{N}/\mathrm{m}$, and ratios up to 4 are obtained experimentally with the considered setup.

Though they are promising, the results of this work underline also several future works to improve the control of TDCR buckling. First, some assumptions we made for the stability analysis need to be relaxed to improve our knowledge of these behaviors. We will investigate the influence of static friction in detail, considering stick and slip regimes, and extend these results to TDCR evolving in space. Second, all the possible configurations of TDCRs should be identified, which implies upgrading our numerical analysis framework with global search algorithms. Third, improved and new strategies must be developed to exploit the buckling phenomena. The prototype and the tendon tension control should be refined in order to achieve a larger reduction of the robot stiffness. Also, new path-planning methods must be developed, to transition between the multiple stable configurations of the robot. This will eventually lead to obtaining different kinematic properties which can be used to improve the versatility of TDCRs.

REFERENCES

[1] Y. Gao, K. Takagi, T. Kato, N. Shono, and N. Hata, "Continuum Robot With Follow-the-Leader Motion for Endoscopic Third Ventriculostomy and Tumor Biopsy," *IEEE Transactions on Biomedical Engineering*, vol. 67, no. 2, pp. 379–390, Feb. 2020.

[2] J. Starke, E. Amanov, M. T. Chikhaoui, and J. Burgner-Kahrs, "On the merits of helical tendon routing in continuum robots," in *IEEE/RSJ International Conference on Intelligent Robots and Systems*, Sep. 2017, pp. 6470–6476.

[3] D. Palmer, S. Cobos-Guzman, and D. Axinte, "Real-time method for tip following navigation of continuum snake arm robots," *Robotics and Autonomous Systems*, vol. 62, no. 10, pp. 1478–1485, Oct. 2014.

[4] E. Amanov, T.-D. Nguyen, and J. Burgner-Kahrs, "Tendon-driven continuum robots with extensible sections—A model-based evaluation of path-following motions," *The International Journal of Robotics Research*, vol. 40, no. 1, pp. 7–23, Jan. 2021.

[5] J. Burgner-Kahrs, D. C. Rucker, and H. Choset, "Continuum Robots for Medical Applications: A Survey," *IEEE Transactions on Robotics*, vol. 31, no. 6, pp. 1261–1280, Dec. 2015.

[6] J. Ha, F. C. Park, and P. E. Dupont, "Elastic Stability of Concentric Tube Robots Subject to External Loads," *IEEE Transactions on Biomedical Engineering*, vol. 63, no. 6, pp. 1116–1128, Jun. 2016.

[7] H. B. Gilbert, R. J. Hendrick, and R. J. W. III, "Elastic Stability of Concentric Tube Robots: A Stability Measure and Design Test," *IEEE Transactions on Robotics*, vol. 32, no. 1, pp. 20–35, Feb. 2016.

[8] Q. Peyron, K. Rabenorosoa, N. Andreff, and P. Renaud, "A numerical framework for the stability and cardinality analysis of concentric tube robots: Introduction and application to the follow-the-leader deployment," *Mechanism and Machine Theory*, vol. 132, pp. 176–192, Feb. 2019.

[9] J. S. Kim, D. Y. Lee, K. Kim, S. Kang, and K. J. Cho, "Toward a solution to the snapping problem in a concentric-tube continuum robot: Grooved tubes with anisotropy," in *IEEE International Conference on Robotics and Automation*. Hong-Kong: IEEE, May 2014, pp. 5871–5876.

[10] C. Bergeles, A. H. Gosline, N. V. Vasilyev, P. J. Codd, P. J. d. Nido, and P. E. Dupont, "Concentric Tube Robot Design and Optimization Based on Task and Anatomical Constraints," *IEEE Transactions on Robotics*, vol. 31, no. 1, pp. 67–84, Feb. 2015.

[11] I. Tunay, "Modeling magnetic catheters in external fields," in *International Conference of the IEEE Engineering in Medicine and Biology Society*, Sep. 2004, pp. 2006–2009.

[12] J. Edelmann, A. J. Petruska, and B. J. Nelson, "Magnetic control of continuum devices," *The International Journal of Robotics Research*, vol. 36, no. 1, pp. 68–85, Jan. 2017.

[13] Q. Peyron, Q. Boehler, K. Rabenorosoa, B. J. Nelson, P. Renaud, and N. Andreff, "Kinematic Analysis of Magnetic Continuum Robots Using Continuation Method and Bifurcation Analysis," *IEEE Robotics and Automation Letters*, vol. 3, no. 4, pp. 3646–3653, Oct. 2018.

[14] C. Li and C. D. Rahn, "Design of Continuous Backbone, Cable-Driven Robots," *Journal of Mechanical Design*, vol. 124, no. 2, pp. 265–271, May 2002.

[15] M. Mahvash and P. E. Dupont, "Stiffness Control of Surgical Continuum Manipulators," *IEEE Transactions on Robotics*, vol. 27, no. 2, pp. 334–345, Apr. 2011.

[16] R. E. Goldman, A. Bajo, and N. Simaan, "Compliant Motion Control for Multisegment Continuum Robots With Actuation Force Sensing," *IEEE Transactions on Robotics*, vol. 30, no. 4, pp. 890–902, Aug. 2014.

[17] Y.-J. Kim, S. Cheng, S. Kim, and K. Iagnemma, "A Novel Layer Jamming Mechanism With Tunable Stiffness Capability for Minimally Invasive Surgery," *IEEE Transactions on Robotics*, vol. 29, no. 4, pp. 1031–1042, Aug. 2013.

[18] M. Langer, E. Amanov, and J. Burgner-Kahrs, "Stiffening Sheaths for Continuum Robots," *Soft Robotics*, vol. 5, no. 3, pp. 291–303, Mar. 2018.

[19] C. Chautems, A. Tonazzini, Q. Boehler, S. H. Jeong, D. Floreano, and B. J. Nelson, "A Magnetic Continuum Device with Variable Stiffness for Minimally Invasive Surgery," *Advanced Intelligent Systems*, vol. 0, no. ja, p. 1900086, Sep. 2019.

[20] A. Shiva, A. Stilli, Y. Noh, A. Faragasso, I. D. Falco, G. Gerboni, M. Cianchetti, A. Menciassi, K. Althoefer, and H. A. Wurdemann, "Tendon-Based Stiffening for a Pneumatically Actuated Soft Manipulator," *IEEE Robotics and Automation Letters*, vol. 1, no. 2, pp. 632–637, Jul. 2016.

[21] L. Blanc, A. Delchambre, and P. Lambert, "Flexible Medical Devices: Review of Controllable Stiffness Solutions," *Actuators*, vol. 6, no. 3, p. 23, Sep. 2017.

[22] M. Manti, V. Cacucciolo, and M. Cianchetti, "Stiffening in Soft Robotics: A Review of the State of the Art," *IEEE Robotics & Automation Magazine*, vol. 23, no. 3, pp. 93–106, Sep. 2016.

[23] Y.-H. Chen and C.-C. Lan, "An Adjustable Constant-Force Mechanism for Adaptive End-Effector Operations," *Journal of Mechanical Design*, vol. 134, no. 031005, Feb. 2012.

[24] M. Yalcin, B. Uzunoglu, E. Altintepe, and V. Patoglu, "VnSA: Variable negative stiffness actuation based on nonlinear deflection characteristics of buckling beams," in *2013 IEEE/RSJ International Conference on Intelligent Robots and Systems*, Nov. 2013, pp. 5418–5424.

[25] J. Begey, M. Nierenberger, P. Pfeiffer, S. Lecler, and P. Renaud, "A novel force sensor with zero stiffness at contact transition based on optical line generation," in *International Conference on Robotics and Automation*, May 2019, pp. 8394–8400.

[26] A. Pal, V. Restrepo, D. Goswami, and R. V. Martinez, "Exploiting Mechanical Instabilities in Soft Robotics: Control, Sensing, and Actuation," *Advanced Materials*, vol. 33, no. 19, p. 2006939, 2021.

[27] J. Prechtl, J. Kunze, D. Bruch, S. Seelecke, and G. Rizzello, "Bistable Actuation in Multi-DoF Soft Robotic Modules Driven by Rolled Dielectric Elastomer Actuators," in *IEEE International Conference on Soft Robotics*, Apr. 2021, pp. 82–89.

[28] P. Rao, Q. Peyron, S. Lilge, and J. Burgner-Kahrs, "How to Model Tendon-Driven Continuum Robots and Benchmark Modelling Performance," *Frontiers in Robotics and AI*, vol. 7, 2021.

[29] A. Gao, Y. Zou, Z. Wang, and H. Liu, "A General Friction Model of Discrete Interactions for Tendon Actuated Dexterous Manipulators," *Journal of Mechanisms and Robotics*, vol. 9, no. 4, Aug. 2017, number: 4.

[30] J. Till and D. C. Rucker, "Elastic Stability of Cosserat Rods and Parallel Continuum Robots," *IEEE Transactions on Robotics*, vol. 33, no. 3, pp. 718–733, Jun. 2017.

[31] A. Lazarus, J. T. Miller, and P. M. Reis, "Continuation of equilibria and stability of slender elastic rods using an asymptotic numerical method," *Journal of the Mechanics and Physics of Solids*, vol. 61, no. 8, pp. 1712–1736, Aug. 2013.

[32] S. Briot and A. Goldsztejn, "Singularity Conditions for Continuum Parallel Robots," *IEEE Transactions on Robotics*, pp. 1–19, 2021.

[33] J. Sikorski, A. Denasi, G. Bucchi, S. Scheggi, and S. Misra, "Vision-Based 3-D Control of Magnetically Actuated Catheter Using BigMag—An Array of Mobile Electromagnetic Coils," *IEEE/ASME Transactions on Mechatronics*, vol. 24, no. 2, pp. 505–516, Apr. 2019.

[34] J.-D. Yau, "Closed-form solutions of large deflection for a guyed cantilever column pulled by an inclination cable," *Journal of Marine Science and Technology*, vol. 18, no. 1, pp. 130–136, 2010.
[35] D. C. Rucker and R. J. W. III, "Statics and Dynamics of Continuum Robots With General Tendon Routing and External Loading," *IEEE Transactions on Robotics*, vol. 27, no. 6, pp. 1033–1044, Dec. 2011.
[36] D. Lin, N. Jiao, Z. Wang, and L. Liu, "A Magnetic Continuum Robot With Multi-Mode Control Using Opposite-Magnetized Magnets," *IEEE Robotics and Automation Letters*, vol. 6, no. 2, pp. 2485–2492, Apr. 2021.
[37] J. Li, Y. Zhou, J. Tan, Z. Wang, and H. Liu, "Design and Modeling of a Parallel Shifted-Routing Cable-Driven Continuum Manipulator for Endometrial Regeneration Surgery," in *IEEE/RSJ International Conference on Intelligent Robots and Systems*, Oct. 2020, pp. 3178–3183.
[38] K. Oliver-Butler, J. Till, and C. Rucker, "Continuum Robot Stiffness Under External Loads and Prescribed Tendon Displacements," *IEEE Transactions on Robotics*, vol. 35, no. 2, pp. 403–419, Apr. 2019.
[39] J. Back, R. Karim, Y. Noh, K. Rhode, K. Althoefer, and H. Liu, "Tension Sensing for a Linear Actuated Catheter Robot," in *Intelligent Robotics and Applications*, ser. Lecture Notes in Computer Science. Cham: Springer International Publishing, 2015, pp. 472–482.
[40] S. H. Jeong, K.-S. Kim, and S. Kim, "Designing Anthropomorphic Robot Hand With Active Dual-Mode Twisted String Actuation Mechanism and Tiny Tension Sensors," *IEEE Robotics and Automation Letters*, vol. 2, no. 3, pp. 1571–1578, Jul. 2017.
[41] D. Bombara, S. Fowzer, and J. Zhang, "Compliant, Large-Strain, and Self-Sensing Twisted String Actuators," *Soft Robotics*, vol. 9, no. 1, pp. 72–88, Feb. 2022.

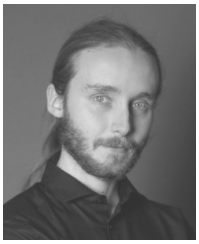

Quentin Peyron (Member, IEEE) received the mechatronic engineer degree in 2016 from INSA Strasbourg, Strasbourg, France, in 2016 and the Ph.D degree in robotics from the University of Bourgogne Franche Comté, Besançon, France in 2019.

He is currently a Researcher at Centre Inria de l'Université de Lille in the DEFormable RObotic SofTware (DEFROST) Team in Lille, France. From 2020 to 2021, he was with the Continuum Robotics Laboratory of the University of Toronto, Canada. His research interests include the modeling, singularity analysis, design and control of deformable robots. He focuses in particular on the eco-design of soft parallel robots, which are promising candidates to tackle social and environmental challenges in robotics.

Jessica Burgner-Kahrs (Senior Member, IEEE) received the Diploma and the Ph.D. degree in computer science from Karlsruhe Institute of Technology (KIT), Karlsruhe, Germany, in 2006 and 2010, respectively.

She is currently an Associate Professor with the Departments for Mathematical & Computational Sciences, Computer Science, and Mechanical and Industrial Engineering, the founding Director of the Continuum Robotics Laboratory (CRL), and an Associate Director of the Robotics Institute, University of Toronto, Canada. From 2013 to 2019, she was with Leibniz University Hannover, Germany and from 2010 to 2012 with Vanderbilt University, Nashville, TN, USA. Her research focus lies on continuum robotics and in particular on their design, modelling, planning and control, as well as human–robot interaction. Her fundamental robotics research is driven by applications in minimally-invasive surgery and maintenance, repair, and operations.